Journal of Electron Spectroscopy and Related Phenomena 222 (2018) 74–87

Contents lists available at ScienceDirect

Journal of Electron Spectroscopy and Related Phenomena

journal homepage: www.elsevier.com/locate/elspec

# 1s2p Resonant Inelastic X-ray Scattering Magnetic Circular Dichroism as a probe for the local and non-local orbitals in $CrO_2$

Patric Zimmermann[a], Nadejda Bouldi[b,c], Myrtille O.J.Y. Hunault[a], Marcin Sikora[e], James M. Ablett[b], Jean-Pascal Rueff[b,d], Blair Lebert[b,c], Philippe Sainctavit[b,c], Frank M.F. de Groot[a,*], Amélie Juhin[c]

[a] Debye Institute of Nanomaterial Science, Utrecht University, 3584 CA Utrecht, The Netherlands
[b] Synchrotron SOLEIL, L'Orme des Merisiers, BP48 Saint-Aubin, 91192 Gif-sur-Yvette, France
[c] Institut de Minéralogie, de Physique des Matériaux et de Cosmochimie (IMPMC), Sorbonne Universités, UMR CNRS 7590, UPMC Univ Paris 06, Muséum National d'Histoire Naturelle, IRD UMR206, 4 Place Jussieu, F-75005 Paris, France
[d] Laboratoire de Chimie Physique-Matiére et Rayonnement, Sorbonne Universités, UPMC Univ Paris 06, CNRS, UMR 7614, F-75005 Paris, France
[e] Academic Centre for Materials and Nanotechnology, AGH University of Science and Technology, 30-059 Kraków, Poland

ARTICLE INFO

*Article history:*
Received 12 November 2016
Received in revised form 22 August 2017
Accepted 25 August 2017
Available online 14 September 2017

*Keywords:*
RIXS-MCD
Magnetic circular dichroism
Non-local
4p3d hybridisation
$CrO_2$
Distortion

ABSTRACT

We have determined the magnetic ground state of the half-metal $CrO_2$ based on 1s2p *Resonant Inelastic X-ray Scattering Magnetic Circular Dichroism* (RIXS-MCD) experiments. The two-dimensional RIXS-MCD map displays the 1s X-ray absorption spectrum combined with the 1s2p X-ray emission decay, where there is a large MCD contrast in the final state involving the 2p core hole.

Our measurements show that the Cr K pre-edge structure is dominated by dipolar contributions and the quadrupole peak is invisible in direct K pre-edge absorption. Using RIXS-MCD, we reveal that the quadrupole 1s3d pre-edge has a large MCD contrast, which appears at lower energy with respect to the K pre-edge maximum.

We use crystal field multiplet calculations to model the excitonic RIXS-MCD spectral shape in tetragonal ($D_{4h}$) symmetry. The RIXS-MCD is strongly sensitive to the ground state distortion of the $Cr^{4+}$ sites. The calculations of the RIXS-MCD maps suggest that the 3d spin–orbit interaction is fully quenched ($\zeta_{3d} = 0$ meV) and the ground state electron configuration must contain a $^3B_{2g}$ ($D_{4h}$) contribution, which is required to explain the appearance of the Magnetic Circular Dichroism (MCD) in the Cr K pre-edge. This is in apparent contrast with the compressed tetragonal distortion.



## 1. Introduction

The detection of the *X-ray magnetic circular dichroism* (XMCD) has become a powerful tool for the element-specific study of the magnetic properties of complex systems. The MCD of 3d transition metal ions is usually studied at the spin–orbit split $L_{2,3}$ absorption edges ($2p \rightarrow 3d$) to allow the determination of the spin and orbital magnetic moments using the sum rules [15,44].

The $L_{2,3}$-edges of 3d transition metals are in the soft X-ray range requiring vacuum conditions, implying that they are difficult for liquid or high-pressure cells. This limits the number of possible applications and the nature of the samples. The energy of the K-edge of 3d transition metals lies in the hard X-ray range, but the direct K-edge MCD signal is weak and the absence of spin–orbit splitting a priori prohibits a quantitative analysis using the spin sum rules.

Some of the above limitations can be addressed with the novel RIXS-MCD approach, in which one combines XMCD and *resonant inelastic X-ray scattering* (RIXS) at the K pre-edge of 3d transition metals according to the following two-step-model (Fig. 1).

$$1s^2\,2p^6\,3d^N \xrightarrow[\text{XAS}]{\circlearrowleft\ \circlearrowright} 1s^1\,2p^6\,3d^{N+1} \xrightarrow[\text{XES}]{} 1s^2\,2p^5\,3d^{N+1}$$

The excitation step (*X-ray Absorption Spectrum*, XAS) is performed with circular polarised light, being either left (lcp, $\circlearrowleft$) or right circular polarised (rcp, $\circlearrowright$). The detection of the subsequent *X-ray emission spectrum* (XES) can in principle also be polarisation

* Corresponding authors.
*E-mail address:* F.M.F.deGroot@uu.nl (F.M.F. de Groot).

https://doi.org/10.1016/j.elspec.2017.08.004

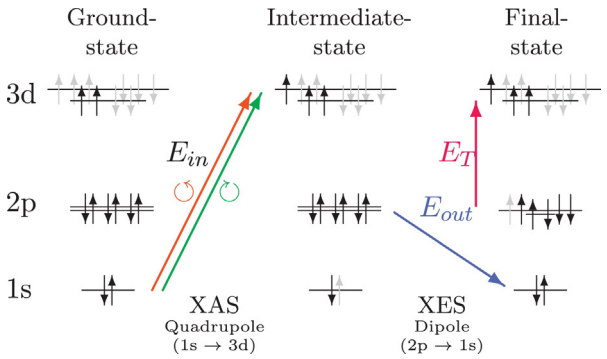


**Fig. 1.** Atomic term scheme for the 1s2p RIXS-MCD photon-in photon-out process for a $3d^2$ electron configuration. $E_{in}$ and $E_{out}$ denote the energies of the incoming and outgoing light, and $E_T$ the energy transferred to the system.

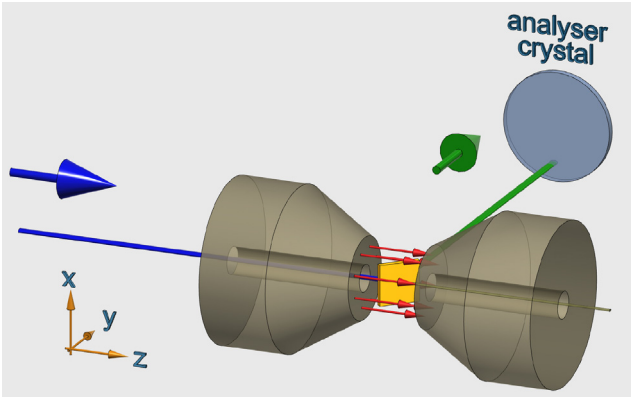


**Fig. 2.** Scheme of the experimental setup with the sample in orange between the two poles of the electromagnet. The circularly polarised incident beam in blue, magnetic field in red and the detected X-ray emission in green. The detector, an *avalanche photo diode* (APD), is not shown for clarity.

dependent, however, for this study no polarisation analyser was used in the XES channel.

RIXS measurements are established to study the electronic structure, while RIXS-MCD additionally offers magnetic information with the advantage that it enhances the contrast of resonant features. The first 1s2p RIXS-MCD experiments have shown that the RIXS-MCD signal of iron in magnetite, can be of the same order of magnitude as $L_{2,3}$-edge XMCD [27,44,51,52]. The RIXS-MCD approach can thus be considered as a high resolution magnetic spectroscopy, while hard X-rays yield bulk sensitivity.

Chromium dioxide ($CrO_2$) is a half-metallic ferromagnet ($T_{Curie} \approx 390\,K$) which means that one spin channel is conductive while the other one is insulating; in other words the electrons in the occupied Cr(3d) bands in $CrO_2$ show nearly 100% spin polarisation [35,40,53]. This makes it a promising candidate for future applications in the field of spintronics [40], for example as a source for spin-polarised currents, magnetic tunnel junctions or other magneto-electronic devices that require a large spin polarisation [60].

The ferromagnetism is usually explained in terms of a specific *double-exchange mechanism* [30,46] related to the existence of the combination of a strongly localised state just below the Fermi level and another dispersed band at higher energy. As Schlottmann states *Hund's rule couples the spin of the localised electron with that of the itinerant electrons and the hopping becomes correlated* [46]. This implies a strong correlation between the spins of the localised and non-localised electrons [46]. The metallicity is due to the dispersed bands that hybridise with the O(2p) bands and cross the Fermi level. This mechanism and the importance of local and non-local correlations is a subject of active research [29].

In spite of the large number of studies, the electronic structure that induces both ferromagnetism and metallicity in $CrO_2$ remains to be understood and *the origin of the half-metallic ferromagnetism is highly nontrivial* [54].

It is expected that RIXS-MCD probes specifically the local magnetic contribution yielding valuable information on the complex electronic structure that leads to metallic ferromagnetism in $CrO_2$. In RIXS-MCD, transitions involving localised d states are expected to give an enhanced intensity with respect to conventional XMCD, while those involving delocalised states are not [52].

RIXS measurements are established to study the electronic structure, while RIXS-MCD additionally offers magnetic information with the advantage that local features appear on resonance with enhanced contrast. The bulk sensitivity of 1s2p RIXS-MCD addresses the common problem of a reduced surface ($Cr^{4+} \rightarrow Cr^{3+}$) in surface sensitive measurements in the soft X-ray range, as in $L_{2,3}$-edge XMCD [2,8,17,18,22,23,28,40] or L-edge RIXS [32].

## 2. Technical details

### 2.1. Experimental setup and measurements

The measured sample is a commercially available crystalline $CrO_2$ powder (MAGTRIEVE™) with a density of $\rho = 4.85\,g/cm^3$ at 25 °C and a grain size of 44 μm (mesh 325) [50]. The powder was milled by hand with mortar and pestle and then pressed into a pill.

The measurements were performed at ambient conditions ($T \approx 25\,°C$, $p \approx 1\,bar$) at the GALAXIES inelastic-scattering beamline at the SOLEIL synchrotron radiation facility [45]. The synchrotron radiation was monochromatised using a Si(111) nitrogen-cooled fixed-exit double-crystal monochromator (DCM) with $\Delta E/E \approx 1.4 \times 10^{-4}$, followed by a Pd-coated spherical collimating mirror. The X-rays were then focused to a spot-size of 30 μm (vertical) by 90 μm (horizontal) full width at half maximum (FWHM) at the sample position by a 3:1 focusing toroidal Pd-coated mirror. A vertical Rowland circle geometry was implemented using a Ge(422) spherical-bent analyser crystal ($R = 1\,m$) which was used to energy-select and focus the emitted X-rays onto a silicon avalanche photodiode detector.

The overall resolution was found to be FWHM ≈ 0.74 eV or $E/\Delta E \approx 7700$ by measuring the quasi-elastic line at 5.4 keV, corresponding to the energy of the Cr $K_\alpha$ fluorescence line. A diamond quarter-wave plate in (111)-orientation with a thickness of $d = 500$ μm, located immediately after the DCM, was used in order to select between left (↺) and right circular polarised (↻) light. An electromagnet created a magnetic flux density $\vec{B}$ of up to $|\vec{B}| \approx 0.7T$ on the sample.

The setup was aligned in longitudinal geometry [31] with $\vec{k} || \vec{B} || \vec{z}$ as shown in Fig. 2. The angles of the sample and the analyser with respect to the incident beam were $\theta = 45°$ and $\theta = 90°$ respectively.

Each measurement was performed with alternating polarisation (lcp↔rcp) for each data point. All spectra were acquired as incident energy scans with the spectrometer fixed to detect a given emission energy $E_{out}$. For the spectra in Fig. 7 the emitted photons corresponding to the Cr $K\alpha_1$ emission at $E_{out} = 5415.3$ eV were detected. For the RIXS maps the detected emission energies were varied accordingly between $E_{out} = 5406$ eV and $E_{out} = 5423$ eV. After completion of a spectrum the direction of the magnetic field was reversed and the measurement repeated. This yields two inverse spectra which are added to minimise noise and reduce systematic errors.

The two-dimensional RIXS maps are displayed either in an *emitted energy view* with the intensity $I(E_{in}, E_{out})$, or in an *energy transfer view* with the intensity $I(E_{in}, E_T)$. The incident energy $E_{in}$ is in both

cases the horizontal $x$ axis, and the $y$ axis is either the emitted photon energy $E_{out}$ or the energy transfer $E_T = E_{in} - E_{out}$. The incident energy $E_{in}$ of the experimental spectra was calibrated against a $CrO_2$ reference [38]. The energies of the emitted photons $E_{out}$ and energy transfer $E_T$ were calibrated with literature values from the *X-ray Data Booklet* (http://xdb.lbl.gov/). The intensities of all spectra are normalised with respect to the sum maximum and given in arbitrary units (a.u.).

### 2.2. Calculations of the densities of states

The *density of states* (DOS) has been calculated using *density-functional theory* (DFT) as implemented in Quantum-Espresso [16], i.e. using a plane-wave basis set, pseudo-potentials and periodic boundary conditions. We used Troullier–Martins [61] norm-conserving pseudo-potentials and the formulation of Perdew–Burke–Ernzerhof [41] (GGA) for the exchange and correlation density functional. The electric dipole and quadrupole contributions to the absorption cross-section are calculated with Xspectra [19,56].

To interpret the experimental spectra, a 1s core hole is added in the calculation. It is described within a static approximation by including a core-hole in the pseudo-potential of the absorbing Cr atom. The Hubbard U correction, whose relevance in the case of $CrO_2$ is discussed in Refs. [6,30,36,58], was not included in the calculation.

The lattice parameters and the dimensionless internal coordinate defining the positions of the atoms were set to their experimental values ($a = b = 4.421$ Å, $c = 2.916$ Å [18,35], $u = 0.303$ [33]). The self-consistent charge density calculation was performed using a centered $6 \times 6 \times 9$ $k$-points grid for the conventional cell that contains one Cr atom and two O atoms. The non-self-consistent calculation is performed with a $12 \times 12 \times 18$ $k$-point grid and the projected density of states are obtained by projecting wave functions onto orthogonalised atomic wave functions. A $2 \times 2 \times 3$ supercell is used to minimise interactions between neighbouring core-holes upon application of periodic boundary conditions and the k-point grid is reduced accordingly.

### 2.3. Crystal-field multiplet calculations

The quadrupole contribution to the pre-edge structure cannot be accurately reproduced with the present DFT-based calculations due to the strong 3d3d correlation effects that determine the pre-edge spectral shape and also the X-ray emission matrix elements. Instead, a crystal-field multiplet (CFM) calculation of the $1s^2\,3d^2 \rightarrow 1s^1\,3d^3$ quadrupole transition with subsequent dipole decay $1s^1\,3d^3 \rightarrow 1s^2\,2p^5\,3d^3$ is applied.

The multiplet calculations are based on the absorption and emission matrices created with the CTM4XAS program [55]. It takes into account all the 3d-3d, 1s-3d and 2p-3d electronic Coulomb interactions, as well as the spin–orbit coupling $\zeta$ on every open shell of the absorbing atom and treats the geometrical environment through a crystal-field potential. All calculations are performed using the $C_4$ point group symmetry to take into account the presence of a magnetic field ($\vec{B}||\vec{k}$). The RIXS process is modelled with the Kramers–Heisenberg relation [44] using additional scripts written for this purpose.

The atomic Slater coefficients for the 3d3d Coulomb interaction $F_{dd}$ are scaled to 65% of the Hartree–Fock values and the 2p3d Coulomb $F_{pd}$ and the exchange interactions ($G_{pd}$, $G_{sd}$) are scaled to 52%. This reduction of the Slater integrals is a result of the expansion of the wave function due to charge transfer effects and the actual values used are an empirical result as they show the best results presented here. The atomic values for the spin–orbit interaction are in the ground state $\zeta_{3d} = 41$ meV, in the intermediate state $\zeta_{3d} = 54$ meV and in the final state $\zeta_{2p} = 5.668$ eV and $\zeta_{3d} = 53$ meV.

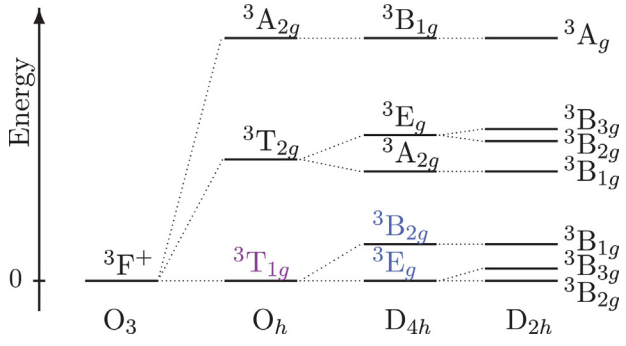


**Fig. 3.** Energy splittings of the multi-electronic state $^3F^+$ for $Cr^{4+}$ ($3d^2$ configuration in high-spin $S = 1$), for each symmetry for $O_3 \rightarrow O_h \rightarrow D_{4h} \rightarrow D_{2h}$ (local exchange is included, but no spin–orbit or magnetic field is taken into account). The order of the energy levels shown above is not fixed. It can be altered in dependency on the specific crystal-field parameters chosen.

For $CrO_2$, there are some reported values for the crystal-field parameter 10D$q$ (Ikeno: 2.28 eV [25], Lewis: 2.5 eV [33]), but we are not aware of any reports for the tetragonal distortion parameters D$s$ and D$t$. Based on the magnitude of the spatial distortion we estimate the two distortion parameters, D$s$ and D$t$, to be of the order of tens of millielectronvolt (meV). The crystal-field parameters (Dq,Ds,Dt) have been varied across a significant section of the parameter space. Only a few representative maps have been chosen to illustrate the general appearance for a given ground state. The displayed calculations refer to the crystal-field splitting parameter 10D$q$ = 2.347 eV and the distortion parameters D$s$ = −0.036 eV, D$t$ = −0.007 eV for $^3E_g$ and D$t$ = −0.2 eV for the $^3B_{2g}$ case. The molecular field $M$ reflecting the interatomic exchange interactions is set to $M = 30$ meV, being estimated with the Curie temperature $T_c \approx 390$ K.

The following Lorentzian broadenings are applied for the intermediate state (IS) $L_{IS} = 1.2$ eV and the final state (FS) $L_{FS} = 0.6$ eV. Here $L_{FS}$ is an intermediate value between the two natural broadenings for the $2p_{3/2}$ and $2p_{1/2}$ final states, corresponding to the K$\alpha_1$ and K$\alpha_2$ emission respectively. As discussed elsewhere [11,14] the lifetime broadening of the $2p_{1/2}$ shell (K$\alpha_2$ line, $L_2$ edge) can be up to five times larger with respect to the $2p_{3/2}$ shell (K$\alpha_1$ line, $L_3$ edge). The experimental (Gaussian) broadening $G_{IS} = 0.7$ eV is set to the experimentally acquired FWHM of the quasi-elastic scattering peak. For the emission, a resolution of $G_{FS} = 0.4$ eV is used. All broadenings are given as full width at half maximum.

Finally, the energy calibration for the theoretical maps is not absolute. The calculated spectra were shifted in both directions for the best agreement with the experimental MCD.

## 3. Theory

### 3.1. Crystal-field multiplet theory

The $CrO_2$ crystal has a rutile structure and belongs to the space-group $P4_2/mnm$ (136) [35,53]. With the metal ion as the inversion center (inversion symmetry) local pd-mixing is forbidden, but mixing between different sites is possible. The $Cr^{4+}$ ions occupy the six-fold oxygen-coordinated sites with Wyckoff position 2$a$ corresponding to $D_{2h}$ point group symmetry [1,18,35,40,53,59,60]. In the ground state, $Cr^{4+}$ in $CrO_2$ has a high spin ($S = 1$) $3d^2$ electron configuration [8], which corresponds to the multi-electronic ground state $^3F^+$ in spherical symmetry ($O_3$) as derived with Hund's rules. The splitting of the atomic multi-electronic state by the crystal-field, through the successive branchings $O_3 \rightarrow O_h \rightarrow D_{4h} \rightarrow D_{2h}$ is illustrated in Fig. 3.

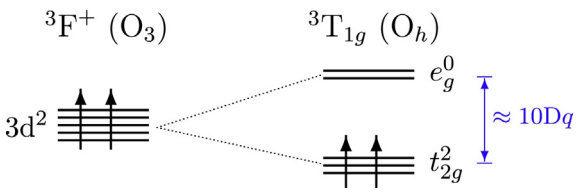


**Fig. 4.** Crystal field splitting of the $3d^2$ high-spin multi-electronic configuration $^3F^+$ ($O_3$), as derived with Hund's rules in spherical symmetry ($O_3$), into the multi-electronic $^3T_{1g}$ ($O_h$) ground state that is dominated by the $|t_{2g}^2\ e_g^0\rangle$ single-electron configuration in octahedral symmetry ($O_h$).

**Table 1**
Metal-ligand distances in the equatorial plane $d_e$ and apex direction $d_a$ for $CrO_2$ from various sources (all values in angstrom ($10^{-10}$m) rounded to the last given digit).

| Reference | $d_e$ | $d_a$ | $d_e - d_a$ |
|---|---|---|---|
| Porta et al. [42] | 1.910 | 1.891 | 0.019 |
| Deng et al. [13] | 1.914 | 1.911 | 0.003 |
| Burdett et al. [5] | 1.911 | 1.888 | 0.023 |
| Baur et al. [3] | 1.917 | 1.882 | 0.035 |
| Average | 1.913 | 1.893 | 0.020 |

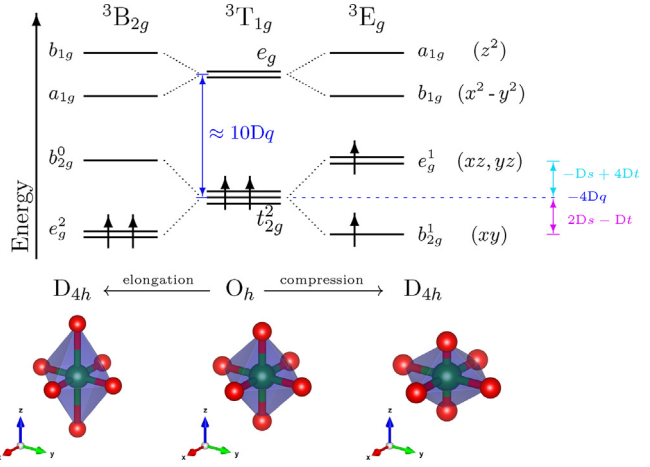


**Fig. 5.** Distortions for a $3d^2$ configuration yielding the transition from octahedral ($O_h$) to tetragonal ($D_{4h}$) symmetry. This changes the multi-electronic $^3T_{1g}$ ($O_h$) ground state into an orbital doublet $^3E_g$ ($D_{4h}$) in case of a compression, and it yields the orbital singlet $^3B_{2g}$ ($D_{4h}$) as the ground state for an axial elongation ($T = 0$ K, no spin–orbit interaction). For the assignment of the energies see Eqs. (1)–(4).

In $O_h$ symmetry only one crystal-field parameter Dq (or 10Dq) is needed. $D_{4h}$ symmetry requires in total three crystal-field parameters (Dq,Ds,Dt), and in $D_{2h}$ symmetry five splitting parameters (Dq,Ds,Dt,$D_\alpha$,$D_\beta$) are required. In Fig. 4, we illustrate in the single-electron picture the splitting of the atomic $3d^2$ orbital into the partially filled and spin-polarised $t_{2g}$, and the empty $e_g$ level in $O_h$ symmetry.

For a tetravalent Cr cation ($Cr^{4+}$) the crystal-field splitting energy 10Dq separating the $t_{2g}$ and the $e_g$ states is estimated (0.6 eV per valency) to be approximately 10Dq ≈ 2.4 eV, in agreement with other reported values (Ikeno: 2.28 eV [25], Lewis: 2.5 eV [33]). The other parameters introduced by lower point group symmetries describe further the splittings of the mono-electronic levels as the consequence from a distortion of the metal ion site.

### 3.2. Importance of the distortion

For $CrO_2$ there are publications dating back to the 1970s [42] reporting a *compression* of the octahedron. The metal-ligand distances in the equatorial plane $d_e$ and the apical distances $d_a$ on the local *z*-axis can be directly acquired from X-ray diffraction (XRD) data. The published values are summarised in Table 1.

Though the difference $d_e - d_a$ varies between 0.3 pm (0.15%) and 3 pm (1.5%) all reports in Table 1 confirm an axial compression. We note that XRD measurements, due to relying on Bragg diffraction, are always an average across many coordination spheres, while the crystal-field model used here is strictly local.

As already pointed out by Korotin et al. [30], the compression of the Cr octahedron induces the further splitting of the $t_{2g}$ orbitals [33,47]. As shown in Fig. 3, a longitudinal compression of the *z*-axis results in the lower point group symmetry $D_{4h}$ and splits the orbital triplet $^3T_{1g}$ ($O_h$) ground state into $^3E_g$ and $^3B_{2g}$ ($D_{4h}$).

In the single particle picture as illustrated in Fig. 5, a compression of the octahedron along its *z*-axis splits the three-fold orbital degenerate $t_{2g}^2$ level ($O_h$, two spin-up electrons in *xy*, *xz*, *yz*) into the $b_{2g}^1$ ($D_{4h}$) level (*xy* orbital) and the *xz*,*yz* orbitals subsequently form the formally half-filled and two-fold orbital degenerate $e_g^1$ ($D_{4h}$) level [46]. In addition, the empty two-fold degenerate $e_g$ ($O_h$) level splits into the $a_{1g}$ ($D_{4h}$) level ($z^2$ orbital) and the $b_{1g}$ ($D_{4h}$) level ($x^2 - y^2$ orbital). Altogether this yields the multi-electronic ground state $^3E_g$ ($D_{4h}$) in the compression case. This situation, with one strongly localised electron in the $b_{2g}$ ($D_{4h}$) level (*xy* orbital) and the second itinerant electron at a higher energy level in the $e_g$ ($D_{4h}$) level is crucial for ferromagnetic $CrO_2$ [13,30,33,46].

This is of great importance because the **double-exchange mechanism** between the Cr ions requires one strongly localised electron in the *xy* orbital and another delocalised and dispersed electron in a higher level mediating the magnetic exchange information (ferromagnetic coupling) via *non-local* transitions [30,46–48].

The spins of the strongly localised electrons in the *xy* orbitals of each Cr site are then coupled via the double-exchange mechanism [30,39,47]. It has been shown that if all electrons were itinerant, an antiferromagnetic coupling would be favoured [48] making the *compression* (meaning the $^3E_g$ groundstate) a requirement to explain the ferromagnetism in $CrO_2$ [47].

On the contrary, in the case of an *elongation* of the octahedrons *z*-axis, the orbital singlet $^3B_{2g}$ ($D_{4h}$) becomes the ground state, where the two 3d electrons are in the $e_g^2$ ($D_{4h}$) level (*xz*, *yz* orbitals) as shown in Fig. 5. In this case, the two electrons are not treated differently, making one localised and one delocalised electron impossible in the elongation case. Hence the ferromagnetism in $CrO_2$ and the distortion of the octahedra are due to this connection closely related.

These considerations highlight that the nature of the Cr site distortion and the relative energies of the electronic levels of the $Cr^{4+}$ ion have a subtle, yet critical, relationship. To approximate the relative energies of the 3d orbitals in the single-particle picture using the three crystal-field parameters Dq, Ds and Dt in tetragonal ($D_{4h}$) symmetry, we use the following set of formulae [9,43]:

$$E_{a_{1g}} = +6Dq - 2Ds - 6Dt \ (d_{z^2} \text{ orbital}) \quad (1)$$

$$E_{b_{1g}} = +6Dq + 2Ds - Dt \ (d_{x^2-y^2} \text{ orbital}) \quad (2)$$

$$E_{e_g} = -4Dq - Ds + 4Dt \ (d_{xz}, d_{yz} \text{ orbital}) \quad (3)$$

$$E_{b_{2g}} = -4Dq + 2Ds - Dt \ (d_{xy} \text{ orbital}) \quad (4)$$

Usually $d_a$ and $d_e$ are of the order of angstroms ($10^{-10}$ m) yielding for |Dq| values of the order of ~100 meV, and |Ds| and |Dt| are usually <100 meV. The expressions (1)–(4) are an approximation in the sense that they consider the crystal-field effects due to the Coulomb interaction between the ion and the ligands, but they entirely disregard local spin–orbit and non-local exchange interactions. However, they are useful to derive the general behaviour in a single-particle picture for a given parameter set (Dq, Ds, Dt).

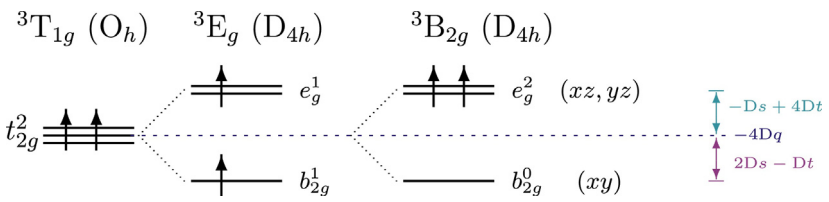


**Fig. 6.** Examples illustrating possible $^3B_{2g}$ ($D_{4h}$) and $^3E_g$ ($D_{4h}$) contributions in the compression case. The picture is restricted to the three $t_{2g}$ ($O_h$) orbitals (*xy*,*xz*,*yz*) leaving the $e_g$ ($O_h$) orbitals empty yielding a total of 9 micro states: 6 for $^3E_g$ ($D_{4h}$) and 3 for $^3B_{2g}$ ($D_{4h}$).

Although the exact point group symmetry of the Cr ions is $D_{2h}$, the $D_{2h}$ splittings are by far too small to be resolvable in the present experimental data. Furthermore the two additional parameters in $D_{2h}$ are essentially unknown, making an evaluation of the crystal-field parameters difficult. Therefore, in the present paper we use $D_{4h}$ symmetry as an approximation in all calculations. In other words, the two $D_{2h}$ parameters $D_\alpha$, $D_\beta$ are implicitly set to zero. For an accurate assessment of the two additional $D_{2h}$ parameters based on experimental data a high resolution of a few millielectronvolt (meV) is required.

Often apical compressions and elongations are discussed as a so called *Jahn–Teller distortion* describing the change of symmetry from $O_h$ to $D_{4h}$. Jahn–Teller distortions arise when the ground state energy can be reduced due to the distortion and hence it has a stabilising effect. However, for $CrO_2$ we note that the point group symmetry is not due to a Jahn–Teller distortion, because this would induce an axial elongation for a $3d^2$ system, where in fact an axial compression is observed. An axial elongation due to Jahn–Teller would lead to the energy stabilised $^3B_{2g}$ ($D_{4h}$) ground state corresponding to a double occupied $e_g$ level (see Fig. 5). In other words the axial compression in $CrO_2$ is not a Jahn–Teller distortion, instead another mechanism is required to justify the stabilisation of the observed compression.

### 3.3. $Cr^{4+}$ ground states $^3E_g$ ($D_{4h}$) and $^3B_{2g}$ ($D_{4h}$)

The two multi-electronic states, the 3-fold (spin) degenerate $^3B_{2g}$ ($D_{4h}$) and the 6-fold degenerate $^3E_g$ ($D_{4h}$), have formally the lowest ground state energy, for an elongation and compression respectively. Hence, at absolute zero $T = 0$ K these are therefore the corresponding ground states (see Fig. 5). However, using only the lowest multi-electronic ground state $^3E_g$ ($D_{4h}$) for the expected compression implies a temperature of $T = 0$ K. The partial term scheme in Fig. 6 illustrates that the multi-electronic state $^3B_{2g}$ ($D_{4h}$), corresponding in the single electron picture to the two electrons in a $|e_g^2\rangle$ configuration, is also one of the excited states in the compression case.

Comparing Figs. 5 and 6 also shows that possible $^3B_{2g}$ ($D_{4h}$) contributions from an excited state in the compression case can be possible. The multi-electronic ground state GS is in this example an unknown linear combination of the $^3B_{2g}$ ($D_{4h}$) and $^3E_g$ ($D_{4h}$) configurations as schematically formalised in expression (5):

$$GS = \alpha \cdot {}^3B_{2g} + \beta \cdot {}^3E_g \tag{5}$$

However, it shall be clear that this is yet simplified and the real linear combination directly relates to the exact multiplet structure, and the result therefore depends on the specific distortion and on the magnetic splitting energies as well as spin–orbit and exchange interactions. In other words, the linear combination depends on the exact order and energy splittings of the individual states due to the various interactions.

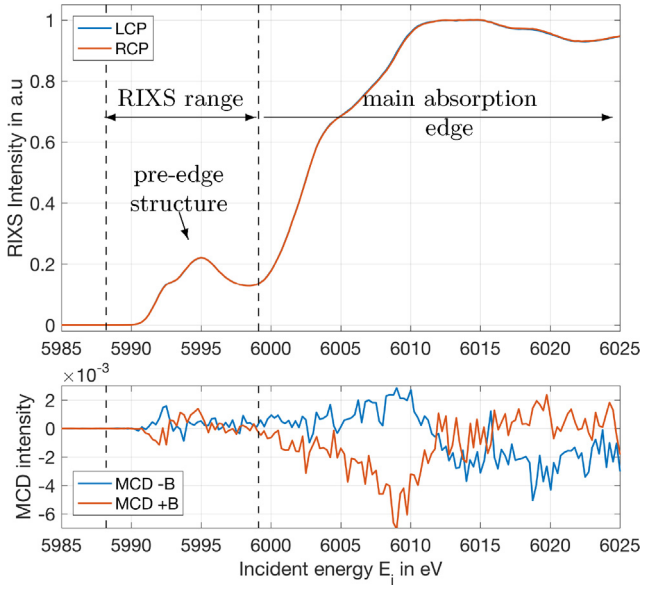


**Fig. 7.** Experimental *High Energy Resolution Fluorescence Detection Magnetic Circular Dichroism* (HERFD-MCD) spectra at the Cr K-edge on $CrO_2$, for $E_{out} = 5415.3$ eV, illustrating the low MCD intensity in the pre-edge ($E_{in} \approx 5992$ eV) and in the dipole main edge ($E_{in} \geq 5998$ eV).

To consider temperatures $T > 0$ K the effective spectrum is commonly approximated as a linear combination of all contributing ground states according to the

**Boltzmann** distribution $p_i \propto \exp\left(\frac{-E_i}{k_B T}\right)$ (6)

where the occupation probability $p_i$ for the multi-electronic state $i$ depends, with the Boltzmann constant $k_B$ and energy $E_i$, on the absolute temperature $T$.

Due to the fact that in $CrO_2$ several energy splittings in the tens of meV lead to a complex multiplet structure, it is without additional information impossible to determine the exact linear combination of the actual ground state. Additionally local and non-local mixing add further difficulties when identifying the ground state character. This can be illustrated with energy level diagrams showing the dependency of the energy levels on the crystal-field parameters D*q*, D*s*, D*t* and *M* (see Fig. 21 in the Appendix).

In this paper we discuss, based on crystal-field multiplet calculations, the different characters of the RIXS and RIXS-MCD maps for two characteristic contributions for the $^3B_{2g}$ ($D_{4h}$) and $^3E_g$ ($D_{4h}$) ground states. The crystal-field multiplet approach without additional charge transfer is a *local* theory, that we use here to model the effect of the local point group symmetry on the splittings of the multi-electronic energy levels of $Cr^{4+}$ ions ($3d^2$). In other words, we calculate only the local contributions explicitly, while non-local hybridisation (charge transfer) is approximated by the reduction of the Slater integrals [10].

Hence it is expected that the calculated sum pre-edge spectrum (Sum = ↻ +↻ ) will lack any intersite transitions or metal-to-

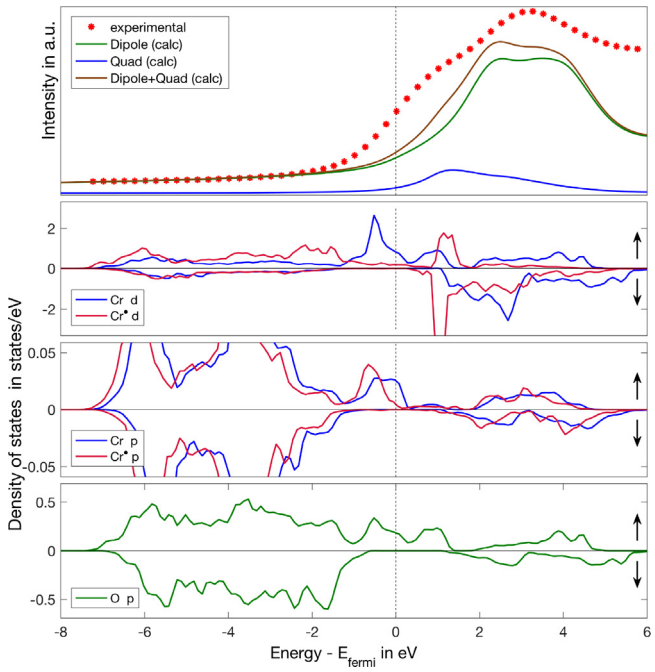


**Fig. 8.** Electric dipole and quadrupole contributions to the absorption cross-section for incident $\vec{k} = (0, 0, 1)$ and polarisation $\vec{\varepsilon} = (1, 0, 0)$, and calculated densities of states (DOS) in $CrO_2$ for the ground state and with a core hole in the Cr 1s shell (indicated as Cr•). Relative contributions of the electric dipole and quadrupole transitions to the pre-edge structure (top), and projected densities of states (DOS) in $CrO_2$ for both spin directions. The Fermi level lies in a gap of the minority spin states and it is fully spin-polarised. Cr(4p),Cr(3d) and O(2p) are overlapping in energy and considered as contributions to the intersite Cr(4p)—O(2p)—Cr(3d) band.

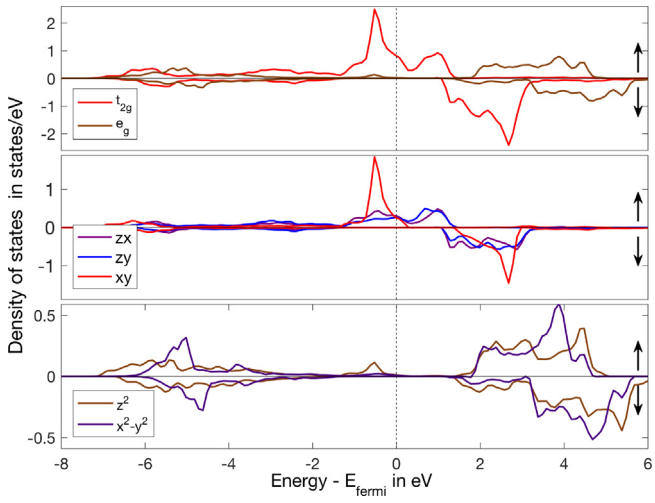


**Fig. 9.** Partial projected Cr(3d) densities of states near the Fermi level. The *xy* orbital appears very localised and lowest in energy being in agreement with the expected compression.

ligand charge transfer and will therefore not be able to reproduce the experimental RIXS map for the sum correctly. However, it is assumed that RIXS-MCD probes a local property, the local magnetic moment, and should therefore be well reproducible within a crystal-field multiplet approach.

## 4. Results and discussion

### 4.1. Chromium K-edge

The *X-ray Absorption Near Edge Structure* (XANES) measured with *High Energy Resolution Fluorescence Detection* (HERFD) at the Cr K-edge are shown in Fig. 7. It covers the Cr K pre-edge region and the main edge, corresponding to a 1s X-ray absorption scan while the spectrometer (analyser angle) remains fixed in order to detect the Cr K$\alpha_1$ ($E_{out}$ = 5415.3 eV) emission that has been calibrated far from resonance.

The dichroism (Fig. 7 bottom) confirms the general trend of two inverted MCD signals for the positive and negative magnetic field direction and it illustrates how small the MCD signal in the pre-edge region really is. The asymmetry between the MCD signals for the two magnetic field directions relates mostly to the relative high noise level as only three scans were averaged. In the following we will look only at the pre-edge structure with incident energies $E_{in}$ < 6 keV.

### 4.2. Density of states

The electric quadrupole and dipole absorption cross-section of the Cr K-edge calculated by first-principle methods (solid lines) is shown in Fig. 8 (top) and compared to the experimental spectrum (dotted line).

In 1s X-ray Absorption Spectroscopy (XAS), the electric dipole transition probes the empty Cr p states whereas the electric quadrupole transition probes the empty Cr d states. From the calculated p and d density of states projected on the Cr atom with a core-hole (Fig. 8, lower 3 plots), we can infer that there is a strong electric dipole contribution between 2 and 5 eV, that is due to the hybridisation of the Cr(4p) states of the absorbing atom with the Cr(3d) states of the neighbouring Cr atoms. Furthermore we find an electric quadrupole contribution at lower energy that appears as a shoulder in the experimental spectra. The main effect of accounting for the onsite Coulomb repulsion through the U term would be an upward shift of the unoccupied d-band [36]. It is known that the energy position of the unoccupied d states near the Fermi level is very sensitive to core hole effects and that, when including a full static 1s core-hole, it is usually calculated at a too high energy with respect to the edge [6]. Hence, the energy separation between the d peak and the p states may not be accurately computed.

In Fig. 9, the Cr(3d) densities are displayed as partial density of states projected onto the corresponding orbitals. The *xy* orbital is localised in energy and thus not part of the continuum, hence it is also localised in real space contrary to the *xz*,*yz* orbitals which are more itinerant, in agreement with the effect of the crystal-field in the compression case. The latter two orbitals (Cr *xz*,*yz*) strongly hybridise with O(2p) states related to the double-exchange mechanism.

Because Cr is centro-symmetric, on-site pd-hybridisation is forbidden by symmetry. Nevertheless intersite hybridisation between the *local* Cr(4p) orbitals and the *non-local* Cr(3d) orbitals of the neighbouring ions is possible (cf. Fig. 7 in [12]). This ***non-local*** or ***intersite*** hybridisation can arise in solids where the many metal sites form bands adding some local Cr(4p) character to the mostly Cr(3d) character of the pre-edge. In $CrO_2$ the O(2p) orbitals mediate the hybridisation between the local Cr(4p) character and the Cr(3d) bands of all Cr sites in the solid to form a "*non-local band*" Cr(4p)—O(2p)—Cr(3d) due to intersite 4p3d hybridisation [12,26,62].

In the ground state, this non-local band overlaps in energy with the Cr(3d) and the Cr(4p) character in the pre-edge. When a 1s core hole, indicated as Cr•, is created the local electronic structure is effectively shifted to lower energy due to the reduced Coulomb repulsion of the core level. The shift of the local Cr•(3d) level with respect to the unchanged Cr(3d) level is expected to be approximately $\Delta E_{in} \approx 2 - -2.5$ eV while the Cr•(4p) level is, due to a

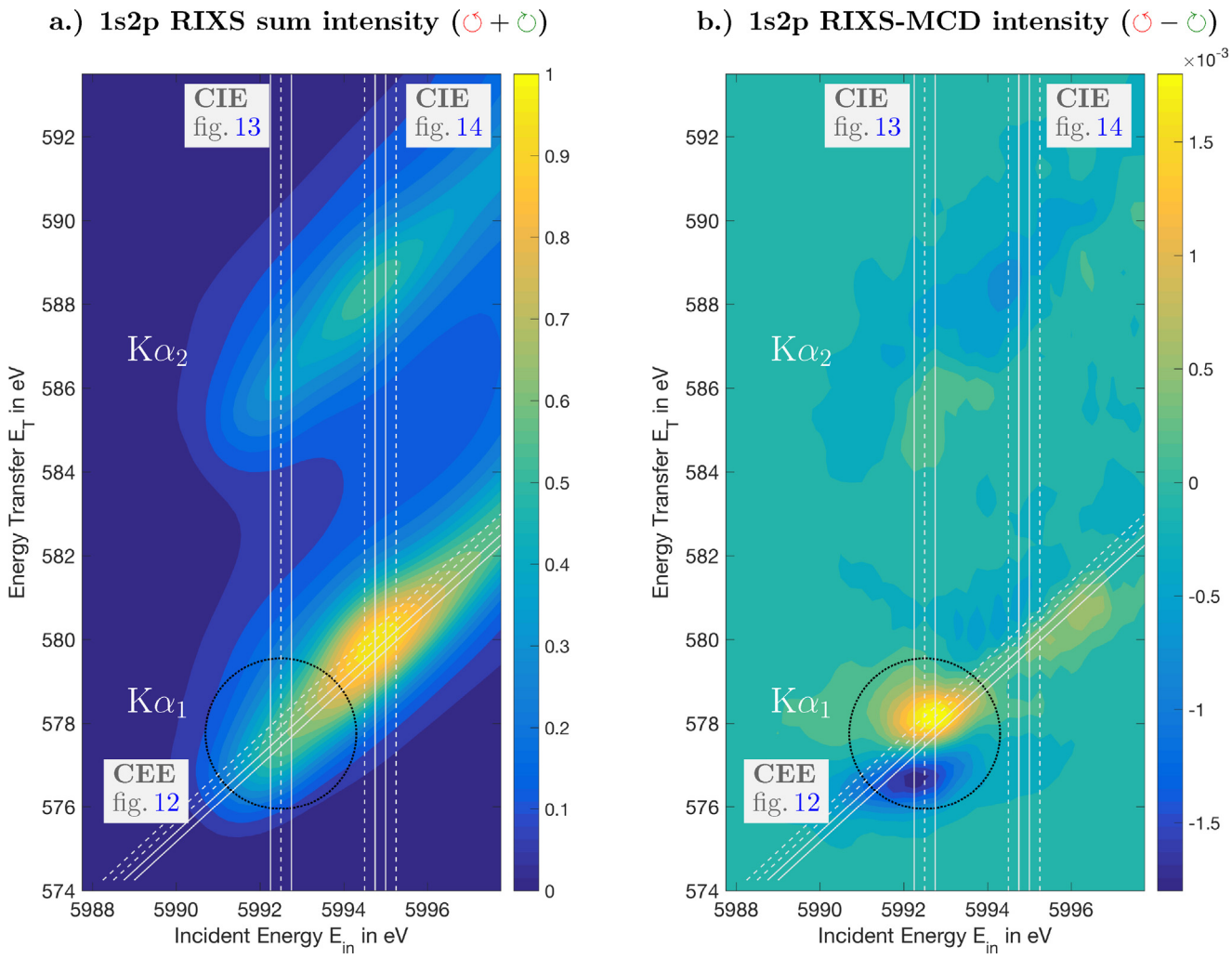


**Fig. 10.** a) Experimental 1s2p RIXS sum (↻+↻) and b) the corresponding RIXS-MCD map (↻-↻) of the $CrO_2$ powder covering the K$\alpha_{1,2}$ doublet, namely the $2p_{3/2} \rightarrow 1s$ (K$\alpha_1$) and $2p_{1/2} \rightarrow 1s$ (K$\alpha_2$) decays after absorption in the Cr K pre-edge. The vertical and diagonal lines highlight the CIE and CEE slices discussed in this paper (see Figs. 12–14).

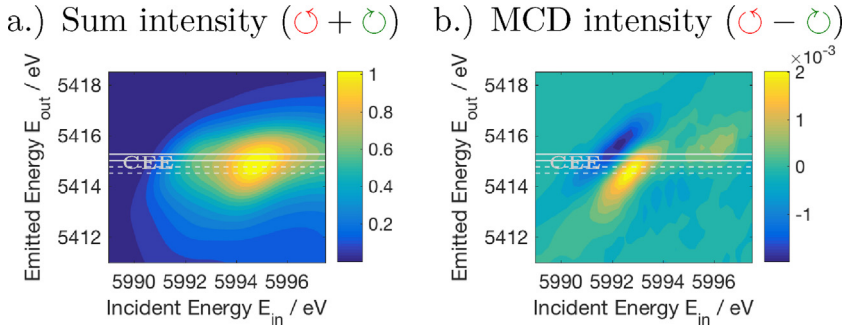


**Fig. 11.** RIXS and RIXS-MCD maps of the K$\alpha_1$ region in an emitted energy view showing the positions of the extracted CEE slices as horizontal lines.

different screening, only slightly shifted by $\Delta E_{in} \approx -0.5$ eV to lower energy [26,62].

All other non-local Cr sites and the non-local band Cr(4p)—O(2p)—Cr(3d) remain essentially unaffected and the pre-edge consists of two types of transitions:

i) Purely local or onsite transitions i.e. the native quadrupole 1s → 3d peak that will appear lowest in energy.
ii) Non-local or intersite transitions i.e. from the local 1s shell into the non-local Cr(4p)—O(2p)—Cr(3d) band which is approximately 2.5 eV above the native Cr•(3d) peak.

This non-local mixing combined with the above described complex order of the multi-electronic ground states makes a detailed analysis of the real electronic configuration difficult.

### 4.3. 1s2p RIXS-MCD map of $CrO_2$

The sum of both circular polarisations (↻ + ↻) yields the 1s2p RIXS map shown in Fig. 10a, and the difference (↻ − ↻) results in the experimental 1s2p RIXS-MCD map of a crystalline $CrO_2$ powder displayed in Fig. 10b.

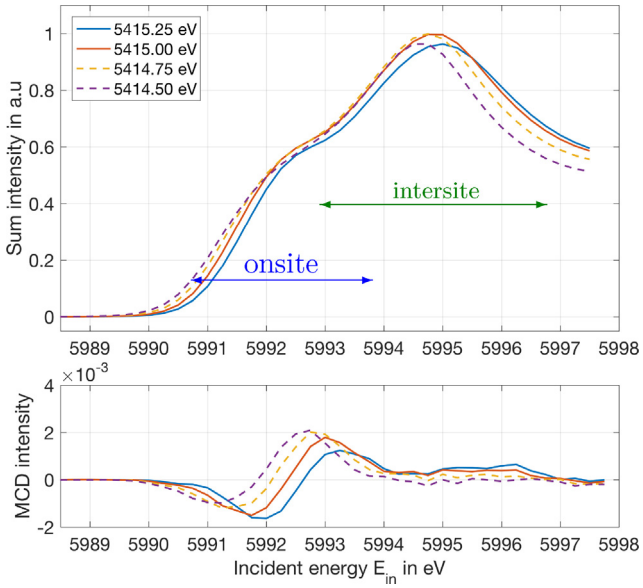


**Fig. 12.** *Constant Emitted Energy* (CEE) slices for $E_{out} \in \{5414.5, 5414.75, 5415.0, 5415.25\}$ eV top: CEE sum slices showing that the K$\alpha_1$ pre-peak clearly consists of multiple peaks; bottom: CEE MCD slices revealing the relative position of the dichroism.

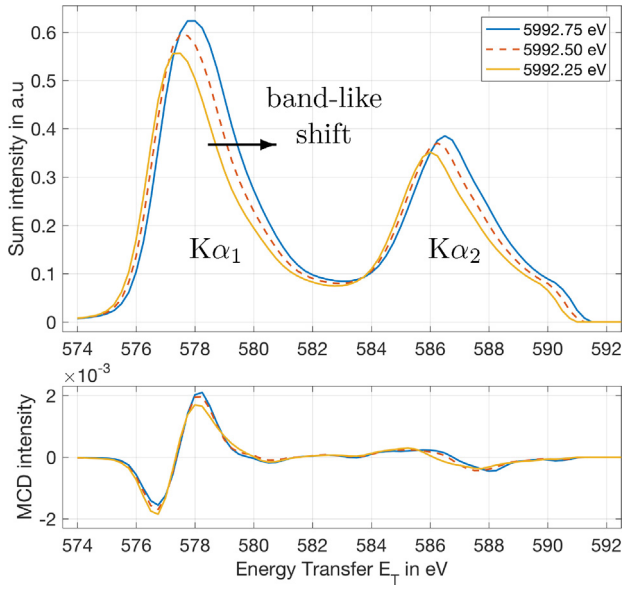


**Fig. 13.** *Constant Incident Energy* (CIE) slices across the onsite region (vgl. Fig. 12) for $E_{in} \in \{5992.25, 5992.50, 5992.75\}$ eV derived from the two maps in Fig. 10. top: CIE sum slices showing the K$\alpha_{1,2}$ doublet; bottom: CIE MCD slices with the strong dichroism for the K$\alpha_1$ emission, while the K$\alpha_2$ region appears only weakly dichroic.

The sum (Fig. 10a) shows the typical band-like diagonal orientation for the K$\alpha_{1,2}$ fluorescence decays. The experimental 1s2p RIXS-MCD map (Fig. 10b) clearly displays an intense magnetic circular dichroism for the $2p_{3/2} \rightarrow 1s$ decay channel (K$\alpha_1$) around $E_T \approx 577$ eV. Its vertical orientation indicates a resonant final state (FS) effect, as opposed to a MCD in horizontal direction would mean resonance on an intermediate state (IS).

The MCD of the $2p_{1/2} \rightarrow 1s$ decay channel (K$\alpha_2$) in the upper half of the map is an order of magnitude less intense with respect to the K$\alpha_1$ dichroism. The K$\alpha_1$ and K$\alpha_2$ regions both display a weak diagonal dichroic background in the MCD map (Fig. 10b).

The K$\alpha_1$ pre-peak maximum in the RIXS map (Fig. 10a) is at $E_{in} \approx 5995$ eV and $E_T \approx 580$ eV while the center of the K$\alpha_1$

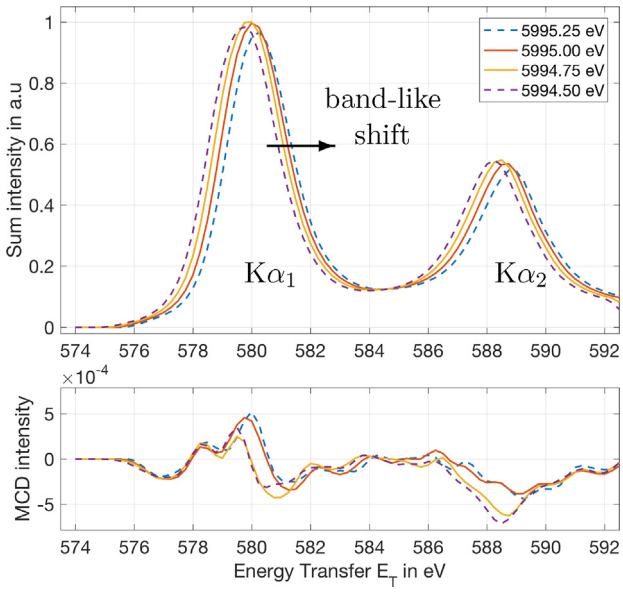


**Fig. 14.** Constant Incident Energy (CIE) slices across the intersite region (vgl. Fig. 12) for $E_{in} \in \{5994.50, 5994.75, 5995.00, 5995.25\}$ eV extracted from Fig. 10. top: CIE sum slices showing the K$\alpha_{1,2}$ doublet; bottom: CIE MCD slices with a relatively weak dichroism for the K$\alpha_{1,2}$ region.

MCD appears approximately at $E_{in} \approx 5992.5$ eV and $E_T \approx 577.5$ eV (Fig. 10b). In other words, the position of the intense K$\alpha_1$ dichroism, marked with a circle in both maps, is located at approximately $\Delta E_{in} \approx 2.5$ eV lower incident energy with respect to the pre-peak maximum of the K$\alpha_1$ emission.

### 4.4. Constant Emitted Energy (CEE) slices

The *Constant Emitted Energy* (CEE) slices are in the following used to investigate the Cr K$\alpha_1$ pre-peak structure. They are comparable to HERFD-XAS and appear as diagonals in a RIXS map in an *energy transfer view* $I(E_{in}, E_T)$. They are identical to the corresponding horizontal slices in maps in an *emitted energy view* $I(E_{in}, E_{out})$. Subsequently, the CEE slices shown as diagonals in Fig. 10 appear as horizontal lines in an *emitted energy view* as displayed in Fig. 11.

These CEE slices correspond to the emitted energies $E_{out} \in \{5414.5, 5414.75, 5415.0, 5415.25\}$ eV. They are shown in Fig. 12 and immediately reveal that the pre-edge structure consists of at least two visible peaks. One peak at $E_{in} \approx 5992$ eV which is assigned to the quadrupole peak ($1s \rightarrow 3d$) giving rise to the MCD, and another structure centred around $E_{in} \approx 5995$ eV is interpreted as a non-local peak, whose contribution to the MCD signal is small.

Therefore, the transitions into the spin-polarised $t_{2g}$ will dominate the MCD [13,24,33]. The empty $e_g$ level however can contribute to the MCD only via the exchange splitting between the spin-up and spin-down $e_g$ states. This seems to be consistent with the MCD appearing at a lower incident energy with respect to the pre-peak maximum as visible in Fig. 12. Here we will use crystal-field multiplet theory in an attempt to calculate the local quadrupole contributions.

### 4.5. Constant Incident Energy (CIE) slices

A vertical slice extracted from a two dimensional RIXS map is a *Constant Incident Energy* (CIE) slice. The CIE slices across the 1s pre-peak are expected to be similar to conventional $L_{2,3}$-edge spectra, because the final state $1s^2\,2p^5\,3d^{N+1}$ is identical in 1s2p RIXS and in 2p XAS. However, the spectra are not identical because the 1s2p RIXS process involves the matrix elements for the $1s \rightarrow 3d$ excita-

tion and the 2p → 1s decay, which are different from the direct 2p XAS matrix elements. Thus the MCD CIE slices across the intense dichroism extracted from the MCD map are expected to be similar but not identical to conventional $L_{2,3}$-edge XMCD spectra [7].

In the following the CIE slices corresponding to the vertical lines in the two maps in Fig. 10 are discussed. The first set of three CIE slices intersecting the intense K$\alpha_1$ dichroism in the **onsite** region at the incident energies $E_{in} \in \{5992.25, 5992.50, 5992.75\}$ eV is displayed in Fig. 13.

As expected, the CIE sum slices in Fig. 13 show the typical band-like shift with increased incident energy $E_{in}$ being consistent with the diagonal appearance of the K$\alpha$ pre-edge emission in Fig. 10a.

The MCD slices on the other hand show only minor differences with no energy shift indicating a resonant (→ excitonic) effect. Only the minima and maxima of the MCD intensity, at $E_T \approx 576.5$ eV and $E_T \approx 578$ eV respectively, vary a bit. This can be explained with the overlapping diagonal band character which is also visible as weak diagonal dichroism in the RIXS-MCD map (Fig. 10b).

Four other CIE slices across the **intersite** region in the maximum of the Cr K$\alpha_1$ pre-edge structure, extracted at the incident energies $E_{in} \in \{5994.50, 5994.75, 5995.00, 5995.25\}$ eV, are displayed in Fig. 14.

The CIE sum slices (Fig. 14 top) are again similar with the typical band-like shift with increased incident energy $E_{in}$. The CIE MCD slices (Fig. 14 bottom) show some energy dependent shift, which indicates that the dichroism in this region, is not purely quadrupolar (→excitonic). The MCD intensities are in this case almost an order of magnitude smaller with respect to the dichroism measured in the low-energy tail of the pre-peak around $E_{in} \approx 5992$ eV as shown in Fig. 13.

The observed energy shift is also consistent with the partially diagonal appearance of the dichroism in the 1s2p RIXS-MCD map (Fig. 10b) around $E_T \approx [580 \pm 1]$ eV. This may be assigned to the non-local mixing of the 3d states inducing some band-like character visible as dipole band transitions into the spin-polarised 3d-band. A detailed quantitative analysis of the dichroism in this intersite region is difficult due to the involved intersite 4p3d hybridisation: this aspect goes beyond the local CFM approach, which does not account for the band structure of the solid and thus it prevents the calculation of transitions to delocalised levels.

It is however noteworthy that overall the K$\alpha_2$ dichroism shows in this experiment no indication of a resonating behaviour as opposed to the K$\alpha_1$ dichroism.

### 4.6. RIXS-MCD ground state character of $CrO_2$

The detailed analysis of the CEE and CIE slices have revealed that the intense dichroism in the experimental RIXS-MCD map in Fig. 10b is dominated by *local* excitonic transitions. Therefore, we assume that the local contributions to the pre-edge sum, and that most of the MCD intensity can be calculated within the local crystal-field multiplet framework.

As discussed above, for ferromagnetic $CrO_2$ an electronic structure corresponding to an axial compression with one strongly localised and one itinerant electron is required for the proposed double-exchange mechanism. The energy level diagram in Fig. 15 shows the behaviour of the multi-electronic states in the case of the compressed distortion of the Cr site for a floating magnetic exchange interaction $M$ and without spin–orbit coupling.

As shown by this diagram, the super-exchange interaction $M$ removes the threefold spin degeneracy of the $^3E_g$ ($D_{4h}$) and $^3B_{2g}$ ($D_{4h}$) terms. The lowest multi-electronic ground state arises from $^3E_g$ ($D_{4h}$) and should therefore dominate the spectrum. The energy $\Delta E$ separating the $^3E_g$ ($D_{4h}$) and $^3B_{2g}$ ($D_{4h}$) at $M = 0$ meV corresponds in this case to $\Delta E = |-3Ds + 5Dt| = 73$ meV and is therefore also dependent on the specific parameter set chosen. In this case

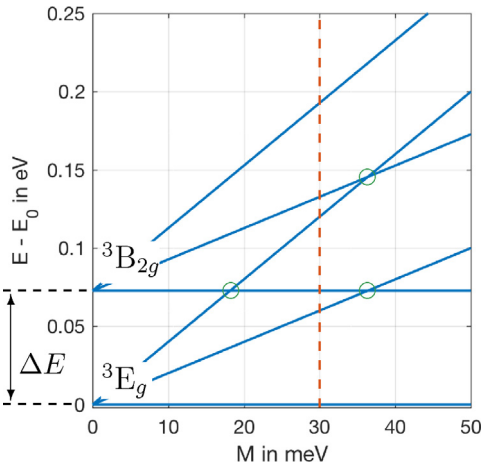


**Fig. 15.** Multi-electronic energy level diagram floating the magnetic exchange parameter $M$ from 0 to 50 meV. The threefold spin degenerate states $^3E_g$ ($D_{4h}$) and $^3B_{2g}$ ($D_{4h}$) are separated at $M = 0$ meV by $\Delta E = |-3Ds + 5Dt| = 73$ meV. The spin degeneracy is then removed due to the magnetic field (→ Zeeman effect). The circles highlight intersections between the states indicating a possible mixing between the states and a change of the ground states order. The dashed line marks $M = 30$ meV used in the calculations.

the splittings are too large to justify a population of $^3B_{2g}$ ($D_{4h}$) states only due to thermal excitation ($T = 300$ K $\rightsquigarrow E = kT \approx 25$ meV).

However, it is important to note that the twofold orbital degeneracy of the $^3E_g$ ($D_{4h}$) state, leading in total to six levels, is not removed here by the magnetic field scaled with $M$. Hence, only the threefold spin degeneracy is removed. This is due to the fact that for ferromagnets one has to use the *Heisenberg exchange coupling* in the Hamiltonian in which the magnetic operator $\hat{O}$ is defined without the orbital momentum $L$:

$$\hat{O} = B_x \cdot (2\,\hat{S}_x) + B_y \cdot (2\,\hat{S}_y) + B_z \cdot (2\,\hat{S}_z) \tag{7}$$

Whereas for paramagnets one has to use the usual definition including the orbital momentum $L$:

$$\hat{O} = B_x \cdot (2\,\hat{S}_x + \hat{L}_x) + B_y \cdot (2\,\hat{S}_y + \hat{L}_y) + B_z \cdot (2\,\hat{S}_z + \hat{L}_z) \tag{8}$$

For both cases, $B_x$, $B_y$, $B_z$ are the components of the magnetic field with $B_x = (1, 0, 0) \cdot M$ (and $B_y$, $B_z$ analog), and $\hat{S}_x$, $\hat{S}_y$, $\hat{S}_z$ are the operators for the corresponding spin components. For the definition in (8) $\hat{L}_x$, $\hat{L}_y$, $\hat{L}_z$ are then analogous the operators for the corresponding orbital components.

As we have to use for the ferromagnet $CrO_2$ the definition in (7), this explains why the twofold orbital degeneracy of the $^3E_g$ ($D_{4h}$) state is not removed in the energy level diagram shown in Fig. 15 (ferromagnet and spin–orbit interaction off). The $^3E_g$ ($D_{4h}$) state will only split into six separate levels (3 for spin, 2 for orbit) when equation (8) is used (paramagnets), or for a ferromagnet with the definition in (7) when spin–orbit interaction is on as shown in the Appendix in Fig. 21 top row.

It would go beyond the scope of this paper to discuss all calculated RIXS-MCD maps that were made to find acceptable agreement with the experimental data. Thus here we present the calculated RIXS-MCD map for a chosen parameter set that corresponds to the compressed distortion, as a benchmark example for the interpretation of the excitonic RIXS and RIXS-MCD features.

#### 4.6.1. RIXS-MCD for $^3E_g$ ($D_{4h}$) ground states

One example calculation for a RIXS and RIXS-MCD map for $^3E_g$ ($D_{4h}$) ground state is shown in Fig. 16 and shortly discussed in the following. The general appearance of the RIXS-MCD map is not similar to the experimental MCD map.

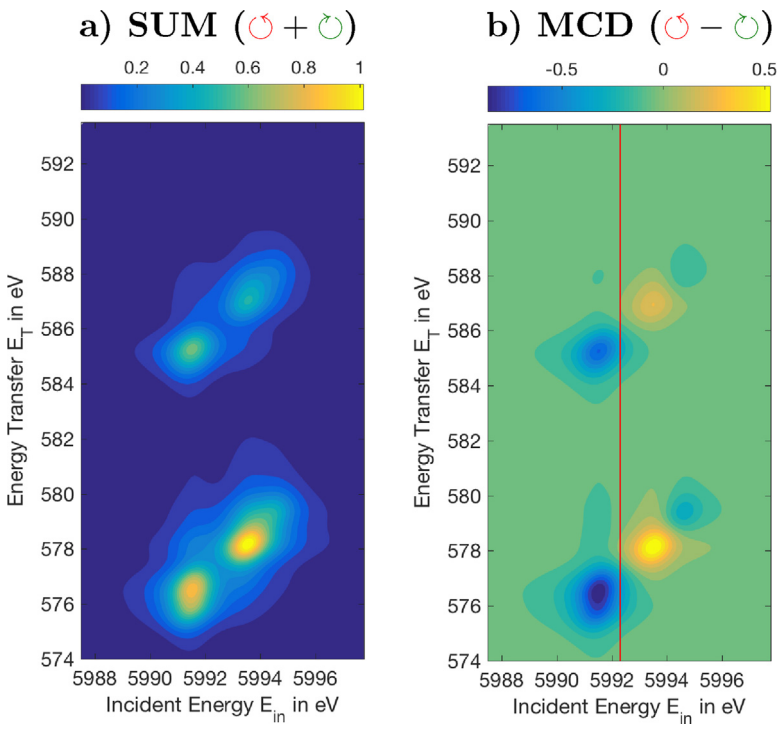


**Fig. 16.** Calculated 1s2p RIXS sum and MCD map for a $^3E_g$ ($D_{4h}$) ground state with spin–orbit coupling $\zeta_{3d}$ = 100%.

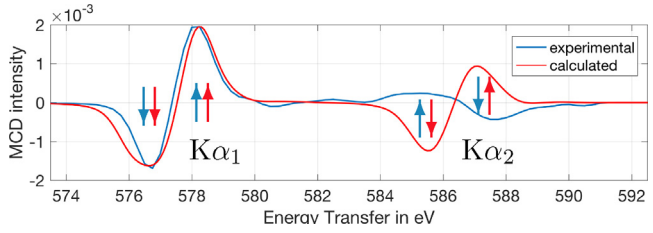


**Fig. 17.** Comparison the MCD CIE slices to visualise the inverted behaviour of K$\alpha_2$ MCD with respect to the K$\alpha_1$ emphasised with arrows indicating the local minima and maxima. The calculated MCD CIE slice is scaled to match the experimental intensity.

Most notable is that the minimum and maximum of the MCD are more separated on both axis when compared to the experimental data. Even under the consideration of the absence of any non-local contributions at higher energies it appears clear that the dichroism is not shifted to the low-energy tail of the pre-edge structure as marked with a circle in the RIXS and RIXS-MCD maps in Fig. 10 and as it is better visible in the CEE slices in Fig. 12.

The CIE slices show the K$\alpha_1$ well reproduced, while the K$\alpha_2$ dichroism apparently has the opposite tendency in the calculation (↓↑ ↓↑ ) with respect to the experimental data (↓↑ ↑↓ ). The red and blue arrows correspond to the local minima and local maximal in the MCD slice and they emphasise the opposite behaviour of the minima and maxima in the MCD of the K$\alpha_2$ region for the comparison between the experimental and calculation data. The effect is also illustrated with arrows in Fig. 17 comparing the calculated CIE slice, which is highlighted by the red line in the RIXS MCD map in Fig. 16b, with the experimental slice already shown in Fig. 13.

This behaviour is visible for essentially all calculated $^3E_g$ ($D_{4h}$) ground states, but because the experimental K$\alpha_2$ MCD appears to be mostly due to non-local mixing, an accurate modelling of the K$\alpha_2$ MCD is beyond the scope of the present multiplet model.

We have performed many calculations across a significant section of the parameter space, and none of the parameter sets for a $^3E_g$ ($D_{4h}$) ground state yields an overall satisfactory result comparable to the experimental data.

#### 4.6.2. RIXS-MCD for $^3B_{2g}$ ($D_{4h}$) ground states

As discussed above $^3B_{2g}$ ($D_{4h}$) corresponds in the single electron picture for $3d^2$ having both electrons in the $e_g^2$ level (*xz*,*yz* orbitals) as displayed in Fig. 5 and Fig. 6. Even though a $^3B_{2g}$ ($D_{4h}$) ground state appears to contradict the requirements for the proposed double-exchange mechanism as cited above [30,46], and it is known that the ground state at absolute zero temperature should be a $^3E_g$ ($D_{4h}$) ground state, our calculations show that we find multiple solutions yielding a RIXS-MCD map comparable to the experimental data for $^3B_{2g}$ ($D_{4h}$) ground states. Furthermore we find that for $^3B_{2g}$ ($D_{4h}$) ground state calculations the RIXS and RIXS-MCD maps are in many cases essentially the same for 3d spin–orbit interaction $\zeta_{3d}$ either on or off.

One example for a calculation for a $^3B_{2g}$ ($D_{4h}$) ground state with 3d spin–orbit interaction set to $\zeta_{3d}$ = 0.0 eV is displayed in Fig. 18.

This is in agreement with other reports finding a reasonably good agreement with spin–orbit interaction effectively switched off due to the vanishing influence of an orbital momentum and correlated spin–orbit effects [49]. Most notable is that the RIXS sum for a $^3B_{2g}$ ($D_{4h}$) ground state in Fig. 18a now consists of two single-peak structures, as opposed to the double-peak structures as visible for the $^3E_g$ ($D_{4h}$) ground state.

A comparison of the calculated RIXS-MCD map in Fig. 18b with the experimental map (Fig. 10b) shows that the weak diagonal dichroism related to the band-character is absent in the calculation. But this is expected and the general appearance of the RIXS-MCD map is quite well reproduced. In fact, under assumption of a $^3B_{2g}$ ($D_{4h}$) ground state we find many solutions similar to the experimental RIXS-MCD map.

In addition we now also find a different behaviour in the CIE slices for the calculation (↓↑ ↓↑ ) with respect to the calculation for the $^3E_g$ ($D_{4h}$) ground state. The results for $^3B_{2g}$ ($D_{4h}$) do in fact

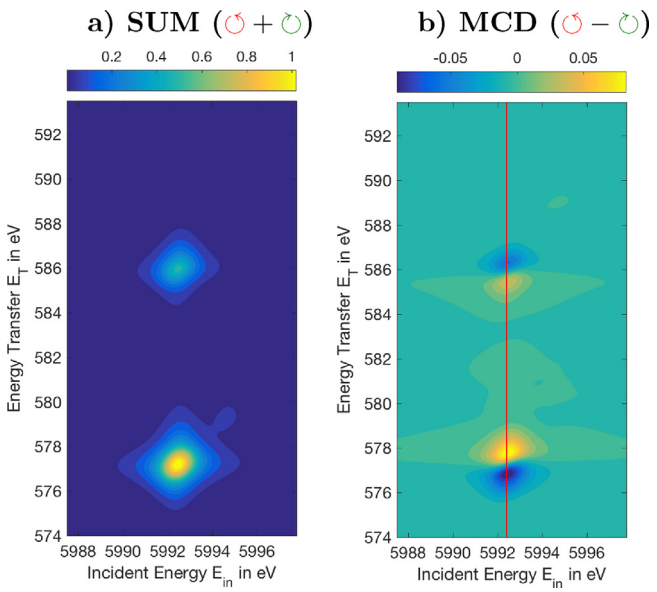


**Fig. 18.** Calculated 1s2p RIXS sum and MCD map for a $^3B_{2g}$ ($D_{4h}$) ground state without spin–orbit interaction $\zeta_{3d} = 0\%$.

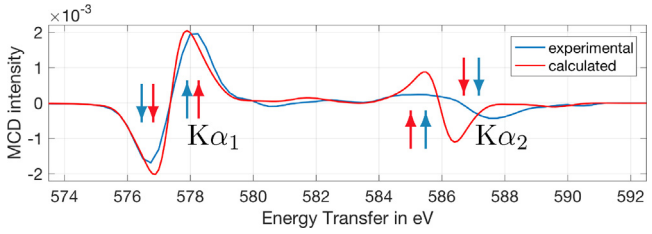


**Fig. 19.** Comparison of the experimental and the calculated CIE slices extracted from Figs. 10b and 18b .(The calculated slice is scaled to match experimental data.)

also agree better with the experimental slices (↓↑ ↑↓ ) as shown in Fig. 19.

Again, it would go beyond the scope of this paper to discuss all calculated RIXS and RIXS-MCD maps for $^3B_{2g}$ ($D_{4h}$) ground states, thus it shall be clear that the shown maps are not supposed to be taken as proposed solutions. Instead the calculations shown here serve only as example to illustrate the general appearance of the RIXS and RIXS-MCD map with a $^3B_{2g}$ ($D_{4h}$) ground state character.

From these calculations, we conclude that the RIXS-MCD signal appears to be dominated by ground state contributions with a $^3B_{2g}$ ($D_{4h}$) character. This would therefore suggest that the ground state is a mixed one, which further triggers the counter-intuitive distortion with respect to pure Jahn–Teller considerations. Such a complex ground state has already been suggested for various systems and in some cases is mediated by both double-exchange mechanism and vibronic couplings, which were not accounted in our present model [4,57].

## 5. Summary

The RIXS-MCD approach delivers valuable information to experimentally disentangle the quadrupole from the dipole contributions, where the quadrupole part of the spectrum reveals magnetic information. As such, hard X-ray RIXS-MCD is a bulk-sensitive high resolution magnetic spectroscopy.

In the case of $CrO_2$ the K pre-edge structure is dominated by dipole transitions into the non-local Cr(4p)—O(2p)—Cr(3d) band originating from intersite 4p3d hybridisation and the quadrupole pre-edge not detectable. The 1s2p RIXS-MCD unravels the strong resonant features in the K$\alpha_1$ dichroism assigned to excitonic states. The non-local states only show a weak non-resonant dichroism.

The assignment of the resonant features in the K$\alpha_1$ dichroism was interpreted with the CFM theory that describes the 3d3d and 2p3d multiplet interactions. Although the compressed axial distortion of the $Cr^{4+}$ octahedron predicts a $^3E_g$ ($D_{4h}$) ground state, the RIXS-MCD calculation of this ground state only fails to reproduce the observed dichroism. Our calculations suggest that i) the spin–orbit coupling of the 3d electrons is quenched, and ii) there is non-negligible contribution from the excited multi-electronic state $^3B_{2g}$ ($D_{4h}$) in the ground state.

We conclude that we cannot give an unambiguous description of the ground state from a local crystal-field approach. Both, the existence of a double-exchange mechanism and the strong non-local Cr(4p)—O(2p)—Cr(3d) hybridisation indicate strong Cr—Cr interactions.

Recent computational developments that enable the coupling between first principle density-functional theory and multi-electronic calculations would enable to go beyond the crystal-field model and provide valuable insights into the nature of the ground state of $CrO_2$.

## Acknowledgements

We wish to acknowledge SOLEIL for provision of the facilities at GALAXIES; explicitly we appreciate the exceptional support from the staff at the GALAXIES beamline at SOLEIL. We thank Pieter Glatzel (ESRF) for lending us the analyser crystal used in this experiment and for sharing his Matlab scripts which were very helpful to write the scripts needed for our calculations.

For financial support we further acknowledge the European Research Council (ERC Advanced Grant 340279). Marcin Sikora (AGH University, Kraków, Poland) acknowledges support from EUSpec COST Action (MP1306) and National Science Centre, Poland (2014/14/E/ST3/00026).

DFT calculations were done using HPC resources from GENCI-IDRIS (Grant i2016096863). The energy level diagrams have been calculated with Quanty (www.quanty.org) [20,34,21]. All molecule structures were created with Vesta [37].

## Appendix A. RIXS-MCD for $^3E_g$ ($D_{4h}$) without spin–orbit interaction

Another set of calculated maps for a $^3E_g$ ($D_{4h}$) ground state with the 3d spin–orbit interaction turned off ($\zeta_{3d} = 0.0$ eV) is shown in Fig. 20. This could be explained with a quenching of the 3d spin–orbit interaction because the atomic value $\zeta_{3d} = 54$ meV is small.

Furthermore the orbital magnetic moments of 3d transition metals are generally quenched because of the crystal-field [28,22,23,18]. The metallicity of $CrO_2$, crystal-field or symmetry effects as well as angular averaging for a powder, all can reduce the spin–orbit interaction.

The general appearance of the RIXS-MCD map is remotely similar to the experimental data, but the MCD intensity is by several orders of magnitude too low ($I_{MCD} \sim 10^{-7}$) with respect to the quadrupole maximum in the sum. Furthermore the dominant MCD of the K$\alpha_1$ region again does not appear in the low energy tail of the pre-edge structure of the RIXS sum, which is the case for the experimental data (see circle in Fig. 10).

Usually it is expected that the 3d spin–orbit interaction $\zeta_{3d}$ separates the MCD minima and maxima in the incident energy $E_{in}$ direction. However, there is clearly a separation of the MCD minimum and maximum also in the incident direction visible in this example proving that it is not purely be the 3d spin–orbit interaction $\zeta_{3d}$.

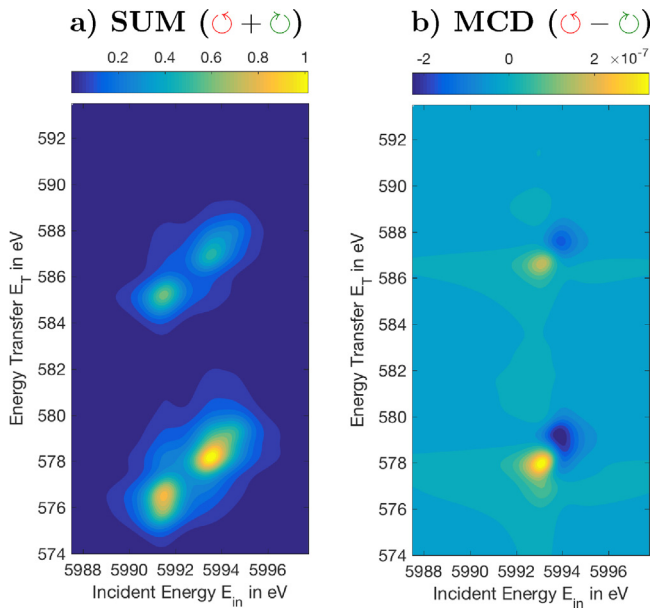


**Fig. 20.** Calculated 1s2p RIXS sum and MCD map for a $^3$E ($D_{4h}$) ground state with 3d spin–orbit interaction $\zeta_{3d}$ off.

## Appendix B. Values used for the calculations

In this part we summarise the values used for the calculations shown in this paper for the *compression case* with the ground state $^3E_g$ (Table 2) and for the *elongation case* for the ground state $^3B_{2g}$ (Table 3).

**Table 2**
Values for the ground state (GS), intermediate state (IS) and final state (FS) for the $^3E_g$ state. Note, the values for spin–orbit interaction $\zeta_{3d}$ are set to 0 meV for the spectra shown in Fig. 20. The results of the calculation are shown in Section 4.6.1 and A.

| | GS | IS | FS |
|---|---|---|---|
| 10D*q* | 2.347 eV | 2.347 eV | 2.347 eV |
| D*s* | −36 meV | −36 meV | −36 meV |
| D*t* | −7 meV | −7 meV | −7 meV |
| *M* | 30 meV | 30 meV | 30 meV |
| $F^2$(2p3d) | – | – | 4.687 eV |
| $G^1$(2p3d) | – | – | 3.508 eV |
| $G^2$(1s3d) | – | 38 meV | – |
| $G^3$(2p3d) | – | – | 1.996 eV |
| $F^2$(3d3d) | 6.133 eV | 6.496 eV | 6.538 eV |
| $F^4$(3d3d) | 3.868 eV | 4.092 eV | 4.123 eV |
| SOC $\zeta_{2p}$ | – | – | 5.668 eV |
| SOC $\zeta_{3d}$ | 41 meV | 54 meV | 53 meV |

**Table 3**
Values for the ground state (GS), intermediate state (IS) and final state (FS) for the $^3B_{2g}$ state. Note, to reflect a fully quenched spin–orbit interaction $\zeta_{3d}$ it is set to 0 meV. The results of the calculation are shown in Section 4.6.2.

| | GS | IS | FS |
|---|---|---|---|
| 10D*q* | 2.347 eV | 2.347 eV | 2.347 eV |
| D*s* | 0 meV | 0 meV | 0 meV |
| D*t* | 200 meV | 200 meV | 200 meV |
| *M* | 30 meV | 30 meV | 30 meV |
| $F^2$(2p3d) | – | – | 4.687 eV |
| $G^1$(2p3d) | – | – | 3.508 eV |
| $G^2$(1s3d) | – | 38 meV | – |
| $G^3$(2p3d) | – | – | 1.996 eV |
| $F^2$(3d3d) | 6.133 eV | 6.496 eV | 6.538 eV |
| $F^4$(3d3d) | 3.868 eV | 4.092 eV | 4.123 eV |
| SOC $\zeta_{2p}$ | – | – | 5.668 eV |
| SOC $\zeta_{3d}$ | 0 meV | 0 meV | 0 meV |

## Appendix C. Energy level diagrams

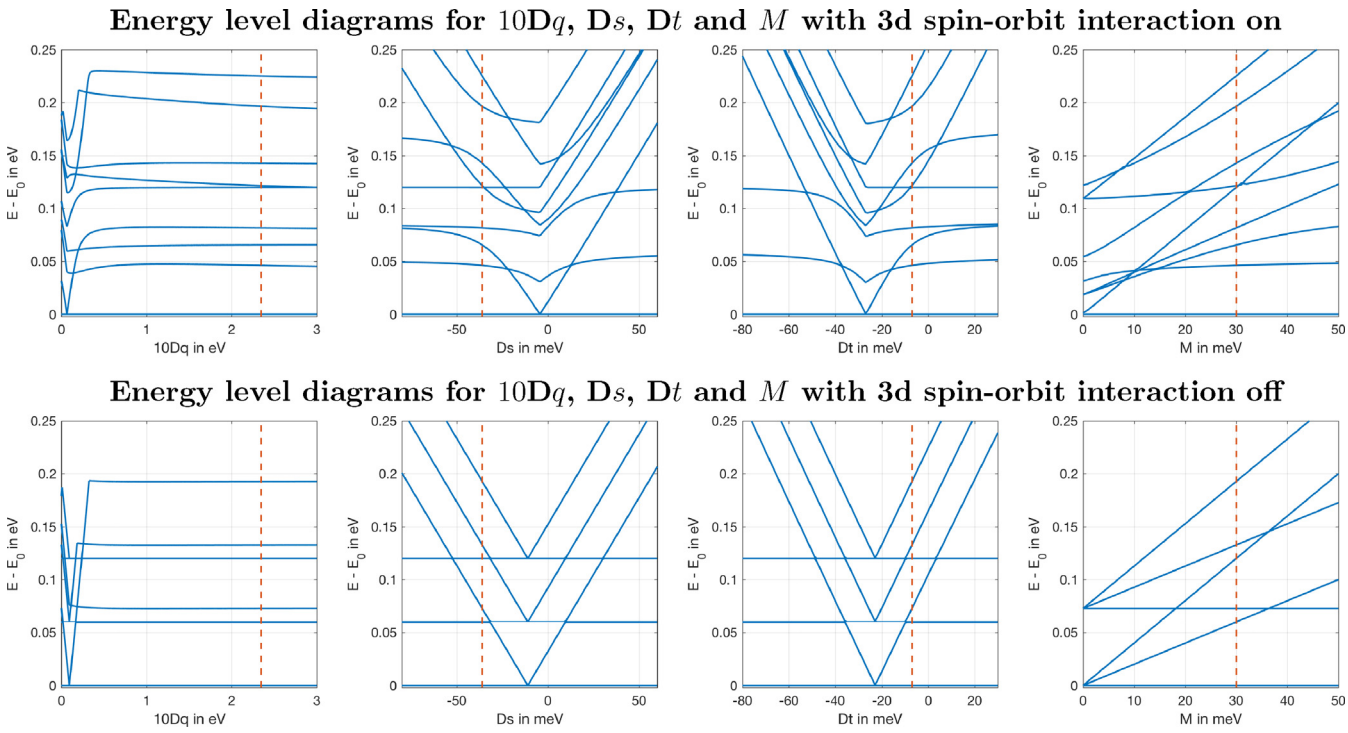


**Fig. 21.** Energy level diagrams for $Cr^{4+}$ with 3d spin–orbit interaction $\zeta_{3d}$ on (top row) and off (bottom row). The vertical red dashed marker lines highlight the approximate value used in the calculation ($10Dq = 2.347$ eV, $Ds = -0.036$ eV, $Dt = -0.007$ eV, $M = 30$ meV). The intersections of the dashed marker line with the energy levels do agree between the four corresponding diagrams and hence enable to illustrate the behaviour in the parameter space in the proximity of the chosen crystal-field and magnetic splitting parameter values. Furthermore it is noteworthy that there are several crossings between the individual states which on the one hand implies a change of the order of the ground states, and on the other hand can indicate a mixing of the ground state characters.

## References


[1] D. Ahlers, K. Attenkofer, G. Schütz, Spin-dependent extended X-ray absorption fine structure in magnetic oxides, J. Appl. Phys. 83 (11) (1998) 7085.

[2] K. Attenkofer, G. Schuetz, Hard and soft X-MCD studies of $CrO_2$, J. Phys. IV France 7 (1997).

[3] W.H. Baur, A.A. Khan, Rutile-type compounds. IV. $SiO_2$, $GeO_2$ and a comparison with other rutile-type structures, Acta Crystallogr. Sect. B 27 (11) (1971) 2133–2139 http://www.crystallography.net/cod/9007540.html.

[4] S.A. Borshch, E.L. Bominaar, G. Blondin, J.J. Girerd, Double exchange and vibronic coupling in mixed valence systems. Origin of the broken-symmetry ground state of $[Fe_3S_4]$ 0 cores in proteins and models, J. Am. Chem. Soc. 115 (12) (1993) 5155–5168.

[5] J.K. Burdett, G.J. Miller, J.W. Richardson, J.V. Smith, Low-temperature neutron powder diffraction study of $CrO_2$ and the validity of the Jahn–Teller viewpoint, J. Am. Chem. Soc. 110 (1988) 8064–8071.

[6] D. Cabaret, A. Bordage, A. Juhin, M. Arfaoui, E. Gaudry, First-principles calculations of X-ray absorption spectra at the K-edge of 3d transition metals: an electronic structure analysis of the pre-edge, Phys. Chem. Chem. Phys. 12 (2010) 5619–5633.

[7] W.A. Caliebe, C.C. Kao, J.B. Hastings, M. Taguchi, A. Kotani, T. Uozumi, F.M.F. de Groot, 1s2p resonant inelastic X-ray scattering in $\alpha$-$Fe_2O_3$, Phys. Rev. B 58 (1998).

[8] C. Chang, D. Huang, A. Tanaka, G. Guo, S. Chung, S. Kao, S. Shyu, C. Chen, Electronic structure of $CrO_2$ studied by magnetic circular dichroism in resonant photoemission, Phys. Rev. B 71 (5) (2005).

[9] F. de Groot, A. Kotani, Core Level Spectroscopy of Solids. Advances in Condensed Matter Science, CRC Press, 2008, ISBN:9781420008425.

[10] F.M. de Groot, X-ray Absorption of Transition Metal Oxides, PhD thesis), University of Nijmegen, 1991, pp. 84ff.

[11] F.M. de Groot, J.C. Fuggle, B.T. Thole, G.A. Sawatzky, $L_{2,3}$ Xray-absorption edges of $d^0$ compounds: $K^+$, $Ca^{2+}$, $Sc^{3+}$, and $Ti^{4+}$ in $O_h$ (octahedral) symmetry, Phys. Rev. B 41 (2) (1990) 928–937.

[12] F.M.F. de Groot, G. Vankó, P. Glatzel, The 1s X-ray absorption pre-edge structures in transition metal oxides, J. Phys.: Condens. Matter 21 (10) (2009) 104207.

[13] Z.-Y. Deng, J.-M. Zhang, K.-W. Xu, The electronic and magnetic properties of the F-doped $CrO_2$ from first-principles study, J. Magn. Magn. Mater. 379 (2014) 196–201.

[14] J.C. Fuggle, B.T. Thole, G.A. Sawatzky, F.M. de Groot, 2p X-ray absorption of 3d transition-metal compounds: an atomic multiplet description including the crystal field, Phys. Rev. B 42 (1990) 5459–5468.

[15] T. Funk, A. Deb, S.J. George, H. Wang, S.P. Cramer, X-ray magnetic circular dichroism – a high energy probe of magnetic properties, Coord. Chem. Rev. 249 (1–2) (2005).

[16] P. Giannozzi, S. Baroni, N. Bonini, M. Calandra, R. Car, C. Cavazzoni, D. Ceresoli, G.L. Chiarotti, M. Cococcioni, I. Dabo, A.D. Corso, S. de Gironcoli, S. Fabris, G. Fratesi, R. Gebauer, U. Gerstmann, C. Gougoussis, A. Kokalj, M. Lazzeri, L. Martin-Samos, N. Marzari, F. Mauri, R. Mazzarello, S. Paolini, A. Pasquarello, L. Paulatto, C. Sbraccia, S. Scandolo, G. Sclauzero, A.P. Seitsonen, A. Smogunov, P. Umari, R.M. Wentzcovitch, QUANTUM ESPRESSO: a modular and open-source software project for quantum simulations of materials, J. Phys.: Condens. Matter 21 (39) (2009) 395502.

[17] E. Goering, A. Bayer, S. Gold, G. Schütz, M. Rabe, U. Ruediger, G. Guentherodt, Strong anisotropy of projected 3d moments in epitaxial $CrO_2$ films, Phys. Rev. Lett. 88 (2002).

[18] E. Goering, M. Justen, J. Geissler, U. Ruediger, M. Rabe, G. Guentherodt, G. Schütz, Magnetic anisotropy of textured $CrO_2$ thin films investigated by X-ray magnetic circular dichroism, Appl. Phys. A: Mater. Sci. Process. 74 (6) (2002).

[19] C. Gougoussis, M. Calandra, A.P. Seitsonen, F. Mauri, First-principles calculations of X-ray absorption in a scheme based on ultrasoft pseudopotentials: from $\alpha$-quartz to high-Tc compounds, Phys. Rev. B 80 (7) (2009) 075102.

[20] M.W. Haverkort, M. Zwierzycki, O.K. Andersen, Multiplet ligand-field theory using Wannier orbitals, Phys. Rev. B 85 (2012) 165113.

[21] M.W. Haverkort, G. Sangiovanni, P. Hansmann, A. Toschi, Y. Lu, S. Macke, Bands, resonances, edge singularities and excitons in core level spectroscopy investigated within the dynamical mean-field theory, EPL (Europhys. Lett.) 108 (5) (2014) 57004.

[22] D. Huang, H. Jeng, C. Chang, G. Guo, J. Chen, W. Wu, S. Chung, S. Shyu, C. Wu, H. Lin, C. Chen, Orbital magnetic moments of oxygen and chromium in $CrO_2$, Phys. Rev. B 66 (17) (2002).

[23] D. Huang, C. Chang, J. Chen, H. Lin, S. Chung, H. Jeng, G. Guo, W. Wu, S. Shyu, C. Chen, Orbital moments of $CrO_2$ and $Fe_3O_4$ studied by MCD in soft X-ray absorption, J. Electron. Spectrosc. Relat. Phenom. 137–140 (2004) 633–639.

[24] D.J. Huang, L. Tjeng, J. Chen, C.F. Chang, W. Wu, S.C. Chung, A. Tanaka, G.Y. Guo, H.J. Lin, S.G. Shyu, C. Wu, C.T. Chen, Anomalous spin polarization and dualistic electronic nature of $CrO_2$, Phys. Rev. B 67 (21) (2003).

[25] H. Ikeno, T. Mizoguchi, I. Tanaka, Ab initio charge transfer multiplet calculations on the $L_{2,3}$ XANES and ELNES of 3d transition metal oxides, Phys. Rev. B 83 (15) (2011) 155107–155114.
[26] A. Juhin, F.M. de Groot, G. Vankó, M. Calandra, C. Brouder, Angular dependence of core hole screening in $LiCoO_2$: a DFT+U calculation of the oxygen and cobalt K-edge X-ray absorption spectra, Phys. Rev. B 81 (11) (2010) 115115.
[27] A. Juhin, A. López-Ortega, M. Sikora, C. Carvallo, M. Estrader, S. Estradé, F. Peiró, M.D. Baró, P. Sainctavit, P. Glatzel, J. Nogués, Direct evidence for an interdiffused intermediate layer in bi-magnetic core–shell nanoparticles, Nanoscale 6 (2014) 11911–11920.
[28] V. Kanchana, G. Vaitheeswaran, M. Alouani, Electronic structure and X-ray magnetic circular dichroism of $CrO_2$, J. Phys.: Condens. Matter 18 (22) (2006) 5155–5162.
[29] M.I. Katsnelson, V.Y. Irkhin, L. Chioncel, A.I. Lichtenstein, R.A. de Groot, Half-metallic ferromagnets: from band structure to many-body effects, Rev. Mod. Phys. 80 (2) (2008) 315–378.
[30] M.A. Korotin, V.I. Anisimov, D.I. Khomskii, G.A. Sawatzky, $CrO_2$: a self-doped double exchange ferromagnet, Phys. Rev. Lett. 80 (19) (1998) 4305–4308.
[31] A. Kotani, Resonant inelastic X-ray scattering and its magnetic circular dichroism, J. Phys. Chem. Solids (2005) 2150–2156.
[32] E. Kurmaev, A. Moewes, S. Butorin, M. Katsnelson, L. Finkelstein, J. Nordgren, P. Tedrow, Half-metallic electronic structure of $CrO_2$ in resonant scattering, Phys. Rev. B 67 (15) (2003) 155105–155114.
[33] S.P. Lewis, P.B. Allen, T. Sasaki, Band structure and transport properties of $CrO_2$, Phys. Rev. B 55 (1997) 10253–10260 arXiv:mtrl-th/9608006.
[34] Y. Lu, M. Höppner, O. Gunnarsson, M.W. Haverkort, Efficient real-frequency solver for dynamical mean-field theory, Phys. Rev. B 90 (2014) 085102.
[35] B. Maddox, C. Yoo, D. Kasinathan, W. Pickett, R. Scalettar, High-pressure structure of half-metallic $CrO_2$, Phys. Rev. B 73 (2006) 144111.
[36] I.I. Mazin, D.J. Singh, C. Ambrosch-Draxl, Transport, optical, and electronic properties of the half-metal $CrO_2$, Phys. Rev. B 59 (1999) 411–418.
[37] K. Momma, F. Izumi, VESTA3 for three-dimensional visualization of crystal, volumetric and morphology data, J. Appl. Crystallogr. 44 (6) (2011) 1272–1276.
[38] S. Ould-Chikh, O. Proux, P. Afanasiev, L. Khrouz, M.N. Hedhili, D.H. Anjum, M. Harb, C. Geantet, J.-M. Basset, E. Puzenat, Photocatalysis with chromium-doped $TiO_2$: bulk and surface doping, ChemSusChem 7 (5) (2014) 1361–1371.
[39] P.W. Anderson, H. Hasegawa, Considerations on double exchange, Phys. Rev. 100 (1955) 675–681.
[40] M. Pathak, Half-metallic $CrO_2$ Thin Films for Spintronic Applications, PhD thesis), University of Alabama, 2011.
[41] J.P. Perdew, K. Burke, M. Ernzerhof, Generalized gradient approximation made simple, Phys. Rev. Lett. 77 (1996) 3865–3868.
[42] P. Porta, M. Marezio, J. Remeika, P. Dernier, Chromium dioxide: high pressure synthesis and bond lengths, Mater. Res. Bull. 7 (2) (1972) 157–161.
[43] S.L. Reddy, T. Endo, G.S. Reddy, Electronic (Absorption) Spectra of 3d Transition Metal Complexes, INTECH Open Access Publisher, 2012 http://cdn.intechopen.com/pdfs/38537/InTech-Electronic_absorption_spectra_of_3d_transition_metal_complexes.pdf.
[44] M. Rovezzi, P. Glatzel, Hard X-ray emission spectroscopy: a powerful tool for the characterization of magnetic semiconductors, Semicond. Sci. Technol. 29 (2) (2014).
[45] J.-P. Rueff, J.M. Ablett, D. Céolin, D. Prieur, T. Moreno, V. Balédent, B. Lassalle-Kaiser, J.E. Rault, M. Simon, A. Shukla, The GALAXIES beamline at the SOLEIL synchrotron: inelastic X-ray scattering and photoelectron spectroscopy in the hard X-ray range, J. Synchrotron Radiat. 22 (1) (2015) 175–179.
[46] P. Schlottmann, Double-exchange mechanism for $CrO_2$, Phys. Rev. B 67 (17) (2003), 174419–7.
[47] P. Schlottmann, Spin exchange in $CrO_2$: the role of a localized level, J. Magn. Magn. Mater. 272–276 (2004) 553–554.
[48] P. Schlottmann, Double exchange and charge fluctuations in CrO2, J. Appl. Phys. 95 (11) (2004) 7471–7473.
[49] G. Schütz, P. Fischer, K. Attenkofer, M. Knülle, D. Ahlers, S. Stähler, C. Detlefs, H. Ebert, F.M.F. de Groot, X-ray magnetic circular dichroism in the near and extended absorption edge structure (invited), J. Appl. Phys. 76 (10) (1994) 6453–6458.
[50] Sigma-Aldrich, Magtrieve Supplementary Information, 2015 http://www.sigmaaldrich.com/catalog/product/aldrich/480037.
[51] M. Sikora, A. Juhin, T.-C. Weng, P. Sainctavit, C. Detlefs, F. de Groot, P. Glatzel, Strong K-edge magnetic circular dichroism observed in photon-in Photon-out Spectroscopy, Phys. Rev. Lett. 105 (3) (2010).
[52] M. Sikora, A. Juhin, G. Simon, M. Zajac, C. Kapusta, L. Morellon, M. Ibarra, P. Glatzel, 1s2p Resonant inelastic X-ray scattering-magnetic circular dichroism: a sensitive probe of 3d magnetic moments using hard X-ray photons, J. Appl. Phys. 111 (7) (2012).
[53] G.P. Singh, S. Ram, J. Eckert, H.-J. Fecht, Synthesis and morphological stability in $CrO_2$ single crystals of a half-metallic ferromagnetic compound, J. Phys.: Conf. Ser. 144 (2009) 012110–012116.
[54] I. Solovyev, I. Kashin, V. Mazurenko, Mechanisms and origins of half-metallic ferromagnetism in $CrO_2$, Phys. Rev. B 92 (14) (2015) 144407–144415.
[55] E. Stavitski, F.M. de, Groot, The CTM4XAS program for EELS and XAS spectral shape analysis of transition metal L edges, Micron 41 (7) (2010) 687–694.
[56] M. Taillefumier, D. Cabaret, A.-M. Flank, F. Mauri, X-ray absorption near-edge structure calculations with pseudopotentials. Application to K-edge in diamond and alpha-quartz, Phys. Rev. B 66 (19) (2002).
[57] B.T. Thole, G. Van Der Laan, P.H. Butler, Spin-mixed ground state of Fe phthalocyanine and the temperature-dependent branching ratio in X-ray absorption spectroscopy, Chem. Phys. Lett. 149 (3) (1988) 295–299.
[58] A. Toropova, G. Kotliar, S.Y. Savrasov, V.S. Oudovenko, Electronic structure and magnetic anisotropy of $CrO_2$, Phys. Rev. B 71 (17) (2005) 172403–172404.
[59] M. Torres Deluigi, F.M. de Groot, G. López-Díaz, G. Tirao, G. Stutz, J. Riveros de la Vega, Core and valence structures in $K_\beta$ X-ray emission spectra of chromium materials, J. Phys. Chem. C 118 (38) (2014) 22202–22210.
[60] D. Tripathy, A. Adeyeye, Electronic properties of field aligned $CrO_2$ powders, Phys. B: Condens. Matter 368 (1–4) (2005) 131–138.
[61] N. Troullier, J.L. Martins, Efficient pseudopotentials for plane-wave calculations, Phys. Rev. B 43 (1991) 1993–2006.
[62] G. Vankó, F.M. de Groot, S. Huotari, R. Cava, T. Lorenz, M. Reuther, Intersite 4p-3d Hybridization in Cobalt Oxides: A Resonant X-ray Emission Spectroscopy Study, 2008, pp. 1–7 arXiv:0802.2744.